Geophysical Journal International

Geophys. J. Int. (2013) **193,** 209–219 doi: 10.1093/gji/ggt002

The processes controlling damage zone propagation induced by wellbore fluid injection

Eyal Shalev and Vladimir Lyakhovsky

Geological Survey of Israel, 30 *Malkhe Israel, Jerusalem,* 95501*, Israel. E-mail: eyal@gsi.gov.il*

Accepted 2013 January 3. Received 2013 January 2; in original form 2012 August 19

SUMMARY

Induced seismicity by wellbore fluid injection is an important tool for enhancing permeability in hydrocarbon and geothermal reservoirs. We model nucleation and propagation of damage zones and seismicity patterns for two-dimensional plane strain configuration at a depth of 5 km using novel numerical software developed in the course of this study. Simulations include the coupling of poro-elastic deformation and groundwater flow with damage evolution (weakening and healing) and its effect on the elastic and hydrologic parameters. Results show that the process occurring during fluid injection can be divided into four stages. The duration of each stage depends on the hydrological and mechanical parameters. Initially, fluid flows into the rock with no seismic events (5 to 20 hr). At this stage, damage increases from 0 to 1 creating two sets of conjugate zones (four narrow damage zones). Thereafter, the occurrence of seismic events and faulting begins and accelerates for the next 20 to 70 hr. At the initial part of this stage, two of the damage zones create stress shadows on the other two damage zones that stop progressing. The velocity of the advancing damage is limited only by the rock parameters controlling damage evolution. At the third stage, which lasts for the following 20–30 hr, damage acceleration decreases because fluid transport becomes a limiting factor as the damage zones are too long to efficiently transfer the pressure from the well to the tip of the damage zones. Finally, the damage decelerates and even stops in some cases. The propagation of damage is controlled and limited by fluid transport from the injection well to the tip of the damage zones because fluid transport does not keep up with the dilatancy of the damage zones. The time and distance of propagation depend on the damage–permeability coupling and the remote shear stress. Higher remote shear stress causes shorter initial periods of no seismicity; strong damage–permeability coupling causes longer acceleration stage.

Key words: Hydrothermal systems; Fracture and Flow; Mechanics, theory, and modeling.

1 INTRODUCTION

Hydraulic stimulation by wellbore fluid injection is widely used to increase permeability in hydrocarbon and geothermal reservoirs (Pearson 1981; Zoback & Harjes 1997; Cuenot *et al.* 2008; Fischer *et al.* 2008; Šílený *et al.* 2009). In the hydrocarbon industry, this technique is used to access and pump trapped oil and gas reservoirs, and in geothermal systems it is used to enhance the ability of fluids to flow in large volumes through high temperature rocks. This process of permeability enhancement is achieved by the creation and growth of damage zones which is accompanied by seismic activity formed by the dynamic failure of the rocks. The magnitude of the seismic events is hard to predict and might reach high values of above three (Häring *et al.* 2008). Although the use of hydraulic stimulation is vast and leads to induced earthquakes, only a few studies have attempted to model the entire process, probably because of its complexity (Tang *et al.* 2002; Adachi *et al.* 2007; Kohl & Megel 2007; Hossain & Rahman 2008; Wang *et al.* 2009; Baisch *et al.* 2010; Lee & Ghassemi 2011; Zhao & Young 2011). Hydraulic stimulation includes: fluid flow, poro-elasticity, brittle failure, seismicity and resulting stress drop, and dependency of the mechanical and hydrological properties on the level of material damage and stress. Only the inclusion of these processes could simulate the creation and growth of damage zones and seismicity that are generated by wellbore fluid injection. The goal of this paper is to model the coupled multiprocesses that occur during hydraulic stimulation and to study the controlling mechanisms of rock failure in different setups using Hydro-Poro-Elastic-Damage (Hydro-PED) software that was developed in the course of this study.

2 FORMULATION

In this study we use continuum damage mechanics (CDM) based on the pioneering works by Robinson (1952), Hoff (1953), Kachanov (1958, 1986), and Rabotnov (1959, 1988). CDM was further developed in engineering (e.g. Hansen & Schreyer 1994; Kachanov 1994; Krajcinovic 1996; Lemaitre 1996; Allix & Hild 2002; Lemaitre & Desmorat 2005) and in earth sciences (e.g. Bercovici *et al.* 2001; Newman & Phoenix 2001; Bercovici & Ricard 2003; Ricard & Bercovici 2003; Shcherbakov & Turcotte 2003; Turcotte *et al.* 2003; Karrech *et al.* 2011). In this study we use the nonlinear viscoelastic damage rheology model of Lyakhovsky *et al.* (1997) and Hamiel *et al.* (2004a,b) that provides a framework for simulating fracturing and faulting processes at various scales. This model accounts for the following general aspects of brittle rock deformation: (1) Nonlinear elasticity that connects the effective elastic moduli to a damage variable and loading conditions; (2) Evolution of the damage state variable as a function of the ongoing deformation and gradual conversion of elastic strain to permanent inelastic deformation during material degradation; (3) Macroscopic brittle instability at a critical level of damage and related rapid conversion of elastic strain to permanent inelastic strain; (4) Coupling between deformation and porous fluid flow through poro-elastic constitutive relationships incorporating damage rheology with Biot's poro-elasticity. This formulation is distinctive in the way that it accounts for the dependency of the mechanical and hydrological properties on damage, and in the formulation of the shear-related dilatancy.

2.1 Solid deformation

The two governing equations are solid force equilibrium and fluid mass conservation. The force equilibrium is given by

$$\sigma_{ij,j} + f_i = 0, \tag{1}$$

where σ_{ij} is the stress tensor and f_i is the body force vector. The poro-elastic constitutive relationship between the stress and strain incorporating damage rheology with Biot's poro-elasticity (e.g. Hamiel *et al.* 2004a) is written as

$$\sigma_{ij} = (\lambda I_1 - \gamma\sqrt{I_2})\delta_{ij} + \left(2\mu - \gamma\frac{I_1}{\sqrt{I_2}}\right)\varepsilon_{ij} - \alpha_B p\delta_{ij}, \tag{2}$$

where $I_1 = \varepsilon_{kk}$ and $I_2 = \varepsilon_{ij}\varepsilon_{ij}$ are the first and second invariants of the elastic strain tensor ε_{ij}, λ and μ are the Lamé parameters of linear Hookean elasticity, γ is a third modulus for damaged solid, α_B is Biot constant, and p is the pore pressure. Below the onset of damage, $\gamma = 0$ and eq. (2) reduces to the Biot linear poro-elastic formulation. With damage, the moduli λ, μ and γ depend on an evolving damage state variable $0 \le \alpha_D \le 1$. The transition from damage accumulation to healing is controlled by the value of the strain invariants ratio $\xi = I_1/\sqrt{I_2}$ which is connected to the internal friction angle of Byerlee's law (Byerlee 1978). The value $\xi = \xi_0$ controls the transition from healing to damage accumulation. The rate of damage/healing accumulation is given by (Lyakhovsky *et al.* 1997)

$$\frac{d\alpha_D}{dt} = \begin{cases} C_d I_2 (\xi - \xi_0) & for \quad \xi > \xi_0 \\ C_1 \exp\left(\frac{\alpha_D}{C_2}\right) I_2 (\xi - \xi_0) & for \quad \xi < \xi_0 \end{cases}, \tag{3}$$

where the coefficient C is the rate of positive damage evolution (material degradation) and is constrained by laboratory experiments (Lyakhovsky *et al.* 1997; Hamiel *et al.* 2004b, 2009). The rate of damage recovery (material healing) is assumed to depend exponentially on α_D and produces logarithmic healing with time in agreement with the behavior observed in laboratory experiments with rocks and other materials (e.g. Dieterich & Kilgore 1996; Scholz 2002; Johnson & Jia 2005). Lyakhovsky *et al.* (2005) showed that the damage model with exponential healing (3) reproduces the main observed features of rate- and state-dependent friction and constrained the coefficients C_1, C_2 by comparing model calculations with laboratory frictional data. The evolving damage state variable α_D is calculated by the integration of $d\alpha_D/dt$ in time. We assume that the elastic moduli depend linearly on damage (Agnon & Lyakhovsky 1995):

$$\lambda = const.$$
$$\mu = \mu_0 + \gamma_r \xi_0 \alpha_D \tag{4}$$
$$\gamma = \gamma_r \alpha_D,$$

where μ_0 is the initial shear modulus and γ_r is constant. Damage (α_D) increase leads to decreasing shear modulus, increasing Poisson ratio, increasing modulus γ, and amplification of the nonlinearity of the effective rock elasticity (eq. 4).

2.2 Seismic events

The damage increase toward its critical level leads to brittle instability and a macroscopic event in one of two modes of failure, tensile and shear failure (Lyakhovsky *et al.* 1997; Lyakhovsky & Ben-Zion 2008). The onset of the brittle instability is triggered by the loss of convexity of the elastic strain energy function, which is mathematically expressed by two conditions (eqs 14 and 15 of Lyakhovsky *et al.* 1997). One condition is realized under moderate damage values and high values of the strain invariants ratio corresponding to tensile stresses. The second condition is realized at higher damage values, but under more compressive loading (see fig. 1 from Lyakhovsky *et al.* 1997). In the first case the mode-I macroscopic failure leads to complete stress drop keeping fluid pressure inside a failed element (hydro-fracturing). This periodically occurs within already developed damage zone that has very low stiffness. As a result, the stress is also low within the damage zone and the pore pressure may exceed the least principal stress. The second mode-II failure condition is modeled by assuming the existence of slipping surfaces within the failed elements, equivalent to a planar fault along which the failing material undergoes frictional sliding (hydro-shearing). Lyakhovsky & Ben-Zion (2008) developed a mathematical procedure for the local stress drop that produces a rapid release of the elastic energy and accumulation of a permanent plastic strain. They utilize the Drucker-Prager model, which generalizes the classical Coulomb yield condition for cohesion-less material. They use scaling relations between the rupture area and seismic potency values established in the seismology and typical range of the stress drop (1–10 MPa) during earthquakes, to calibrate parameters of their local stress drop procedure and connect them to the dynamic friction (~0.2) of simpler models with planar faults. Simulations with the discussed model produce quasi-dynamic stress drops and scaling relations between rupture areas and seismic potency values that are consistent with classical theoretical results and observations summarized by Kanamori & Anderson (1975). Following the mode-II event, the slip associated with the macroscopic brittle failure is arrested and post-failure material healing starts.

2.3 Groundwater flow

The fluid mass conservation equation for saturated isothermal flow is (e.g. Wang 2000)

$$\nabla \cdot \left(\frac{\underline{\underline{\boldsymbol{k}}}(\alpha_D)}{\mu_f}(\nabla p + \rho g \mathbf{z})\right) = S_\varepsilon \frac{\partial p}{\partial t} + \alpha_B \frac{\partial \varepsilon_{kk}}{\partial t}, \tag{5}$$

Table 1. Model parameters and initial conditions.

	Strong damage/ permeability coupling	Weak damage/ permeability coupling	No damage/ permeability coupling
Initial shear stress	30 MPa	40 MPa	40 MPa
k_0	10^{-19} m^2	10^{-19} m^2	10^{-14} m^2
A for damage-free rock	20	12	0
E for damage-free rock		4000 MPa	
ν		0.3	
ξ_0		-0.8	
γ_r		920 MPa	
C_d		10	
C_1		10^{-8}	
C_2		0.03	
α (Biot)		1	
$S\varepsilon$		$5 * 10^{-11}$ 1/Pa	
Initial pore pressure		49 MPa (hydrostatic at 5 km depth)	
Initial lithostatic stress		127.5 MPa (5 km depth)	
Injection pressure		99 MPa (50 MPa overpressure)	

where $\underline{\underline{k}}$ is the intrinsic permeability tensor of the medium, μ_f is the fluid viscosity, ρ is the fluid density of water, g is the gravitational acceleration, z is a unit vector, and S_ε is the specific storage at constant strain. We assume that the permeability depends exponentially on damage (e.g. Picandet *et al.* 2001)

$$\underline{\underline{k}}(\alpha_D) = \underline{\underline{k}}_o * \exp(b\alpha_D), \quad (6)$$

where $\underline{\underline{k}}_o$ is the initial permeability tensor and b is a constant.

2.4 Numerical implementation

This system of equations is solved in state-of-the-art Hydro-PED software, for two-dimensional plane strain conditions. Hydro-PED combines two numerical methods: finite element method (FEM) and explicit finite difference Lagrangian method (EFDLM). Solid deformation is solved with EFDLM and fluid mass conservation is solved using FEM. EFDLM fully explicit numerical method relies on a large-strain explicit Lagrangian formulation originally developed by Cundall (1989). Poliakov *et al.* (1993) developed an adaptive time stepping and developed the EFDLM algorithm to an adaptive scheme that does not require iteration, which makes the numerical model stable even for highly nonlinear damage rheology (Lyakhovsky *et al.* 1993). Another strong feature of EFDLM is that the equations are solved locally without establishment of a global stiffness matrix which allows the elimination of elements that have no stiffness (after tension failure) and for the existence of large variations of stiffness values in neighboring elements. The ability to account for these features is essential for hydraulic stimulation modeling because, as damage develops, the stiffness of the rock (element) changes from its original values of $E = 4{,}000$ MPa when there is no damage to a few MPa when $\alpha_D = 1$, or even to zero when failure is in tension. These features are hard to incorporate in FEM where they cause numerical instabilities. To avoid these instabilities, many FEM codes relate the elastic parameters to strain and not damage. As opposed to the force equilibrium equation with damage, the diffusion equation of the fluid mass conservation is very stable in FEM, and we use it in our formulation. Node coordinates of the numerical mesh are updated every time step as well as shape functions for every triangle element, allowing large strain analyses. The pore pressure used in the eq. 2 is the result of the fluid mass conservation equations and the last term in eq. 4 uses the strain calculated by the force equilibrium subroutine.

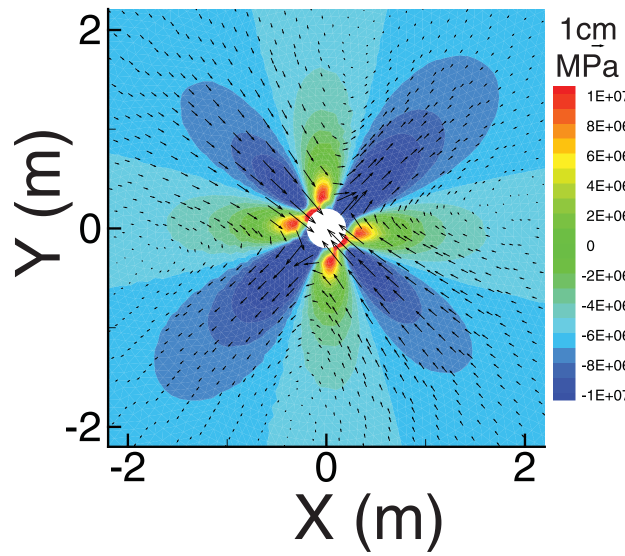

Figure 1. Coulomb failure stress (CFS) on optimally oriented planes around the well, following the formulation of King *et al.* (1994) along with displacements. Positive CFS values indicate the tendency of the rock to fail.

2.5 Model configuration

A circular domain with a radius of 100 m that contains 90,000 triangular elements is used for all simulations. Fluid is injected at the center of the domain into a well with radius of 20 cm. Elements length varies from 5 cm around the injection well to 2 m at the outer circle boundary. The initial principal stresses are: maximum stress – 157.7 MPa, minimum stress – 97.7 MPa, vertical stress – 127.7 MPa. The direction of the principal stress is 45 degrees between the axes. Initial pore pressure of 49 MPa is assigned for the entire domain. These values represent depth of 5 km. Fluid is injected with pressure of 99 MPa (overpressure of 50 MPa). The nodes that define the well have force boundary conditions, whereas the outer boundary has fixed zero displacement conditions. Boundary conditions for the fluid on the outer boundary are zero flux.

Three different simulation scenarios are tested in this study (Table 1). The differences between the simulations are the initially imposed shear stress and the permeability–damage relation parameters (eq. 6). Mechanical and hydrological parameter values represent values of granite (Wang 2000). Initially, the domain is assumed to

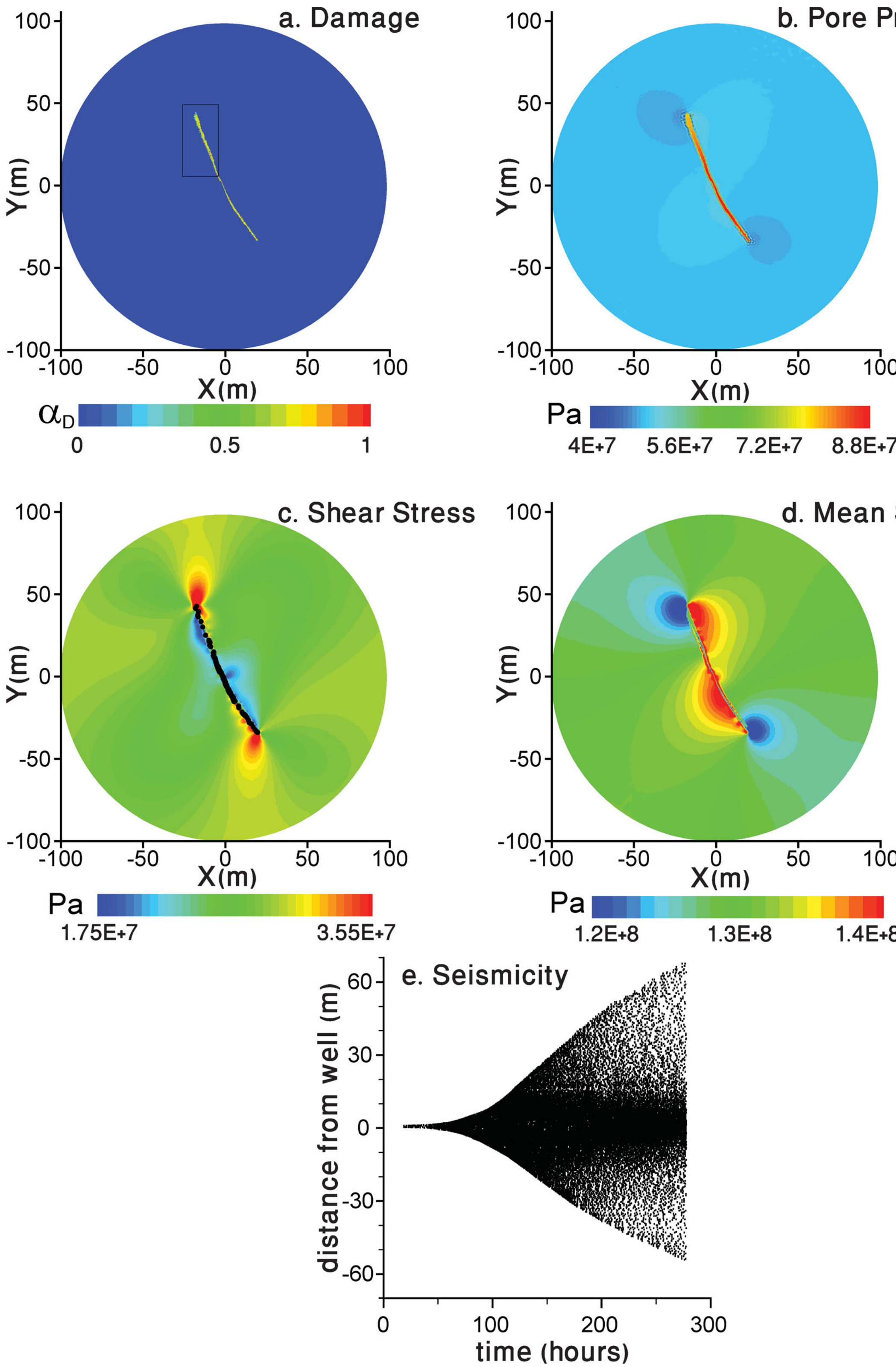

Figure 2. Results of the strong damage–permeability coupling scenario after 200 hr of injection. (a) Damage parameter (α_D), showing the formation of two damage zone. Black box indicates the area shown in Fig. 3. (b) Pore pressure increases mainly within the damage zones by fluid transport from the injection well. Outside the damage zone, the pore pressure changes poro-elastically similar to the pattern changes of the mean stress. (c) Shear stress expressed as the second invariant of the stress tensor (J_2) and seismic events locations. Most of the shear is created at the tips of the damage zones. Seismic events occur only within the damage zones. (d) Mean stress. (e) r-t diagram of seismicity where the slope represent the velocity of damage propagation. Four stages are observed: (1) no seismicity, (2) damage acceleration, (3) constant velocity and (4) damage deceleration.

be homogeneous. Heterogeneous evolutions of the mechanical and hydrological parameters occur as a response to injection. In nature, domains are never homogeneous. Faults and fractures exist to some extent in all sites. This heterogeneity may control initiation and progression of micro-seismic activity. The goal of this study is to understand the physical behavior of the simplest domain. The effect of initial heterogeneity will be examined in future work.

3 RESULTS

The existence of a well (with wellbore pressure) in a sheared environment creates stress clouds with high stress concentration around the well that may trigger the nucleation of the damage (Fig. 1). The proximity of the rock to failure is demonstrated here with the Coulomb failure stress (CFS) on optimally oriented planes around the well, following the formulation of King *et al.* (1994). Positive CFS values indicate the tendency of the rock to accumulate damage leading to macroscopic failure. At very initial stage the damage is accumulated within four areas with high CFS (Fig. 1), but interaction between these areas and stress shading enhances only two of them and stops in the others.

In the case of strong damage–permeability coupling (Table 1), the damage propagates away from the injection well in the center of the circle and creates two damage zones in an angle of 68.5° of the abscissa and 23.5° of σ_1 (Fig. 2a). At an early stage ($t < 30$ hr), two sets of conjugate damage zones are developed forming four damage zones that nucleate at the high CFS areas (Fig. 1), until stress shadows created by one of them stop its conjugate pair (not shown). The pore pressure (Fig. 2b) increases mainly within the damage zone where permeability is high. The initial permeability is set to be 10^{-19} m^2 everywhere, and the creation of damage increases the permeability even at relatively low damage. When the damage increases up to $\alpha_D = 0.58$, the permeability is as high as 10^{-14} m^2 (eq. 6); an increase of five orders of magnitude from the initial value. The only pore pressure changes occurring in the undamaged rock result from poro-elastic effects of the advancing damage zones, similar to the patterns of the mean stress (Fig. 2d). The shear stress is highest at the tip of the damage zones (Fig. 2c). All seismic events occurring are located only within the damage zones (Fig. 2c). The damage zones advance while creating seismic events whenever the damage parameter α_D is equal to one. Therefore, the location of the seismic events over time represents the propagation velocity of the damage zones (Fig. 2e). Seismicity starts after about 20 hr of injection and occurs continuously along the entire damage zones. Damage zone propagation accelerates for 110 hr and then remains at a constant pace for 50 hr before decelerating. These velocities are relatively slow compared to data of field stimulation because flow rates here are also much smaller. If this horizontal cross-section represents a layer with thickness of 500 m then the flow rates are equivalent to 1.2 l/s.

The simulated damage zone does not grow along a straight path (Fig. 3). Instead, a system of left-stepping en-echelon segments, including pull-apart structures that accumulate some amount of dilation, is formed. This kind of deformation was also suggested by Ortiz *et al.* (2011) as the mechanism responsible for sudden pressure drops and changes in hydraulic properties during stimulation. The productivity of seismic events significantly decreases, and damage propagation is stopped immediately after injection is stopped (Fig. 4). After 300 hr there are almost no more seismic events.

In the case of weak damage–permeability coupling and higher initial shear stress of 40 MPa, conditions are more unstable (Fig. 5). Here too, the permeability of the undamaged rock and damaged rock

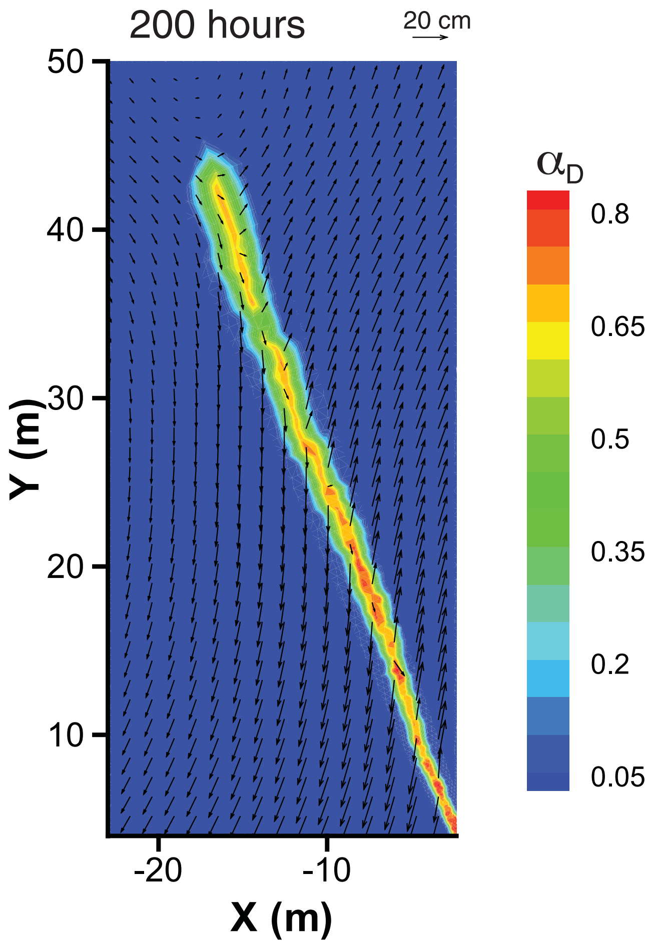

Figure 3. Damage and displacements of the strong damage–permeability coupling scenario after 200 hr of injection. A system of left-stepping en echelon segments is formed. Displacements emphasize the shear that the damage zone is experiencing and the resulting dilation.

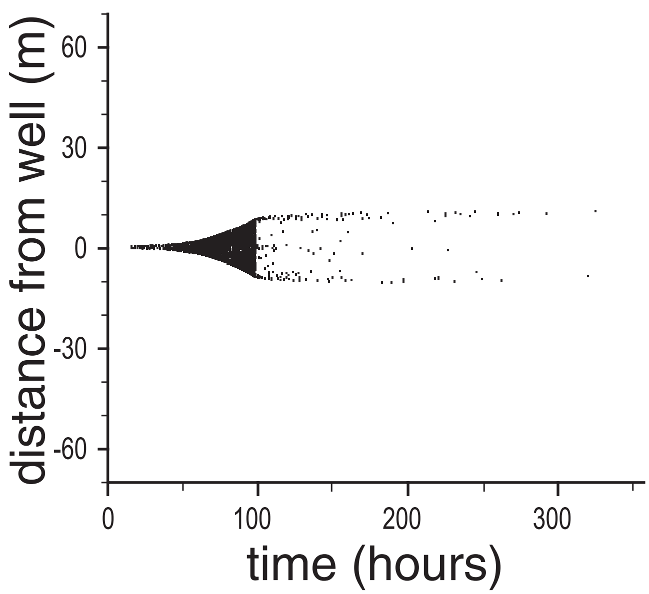

Figure 4. r-t diagram of seismicity in the strong damage–permeability coupling scenario when injection is stopped after 100 hr.

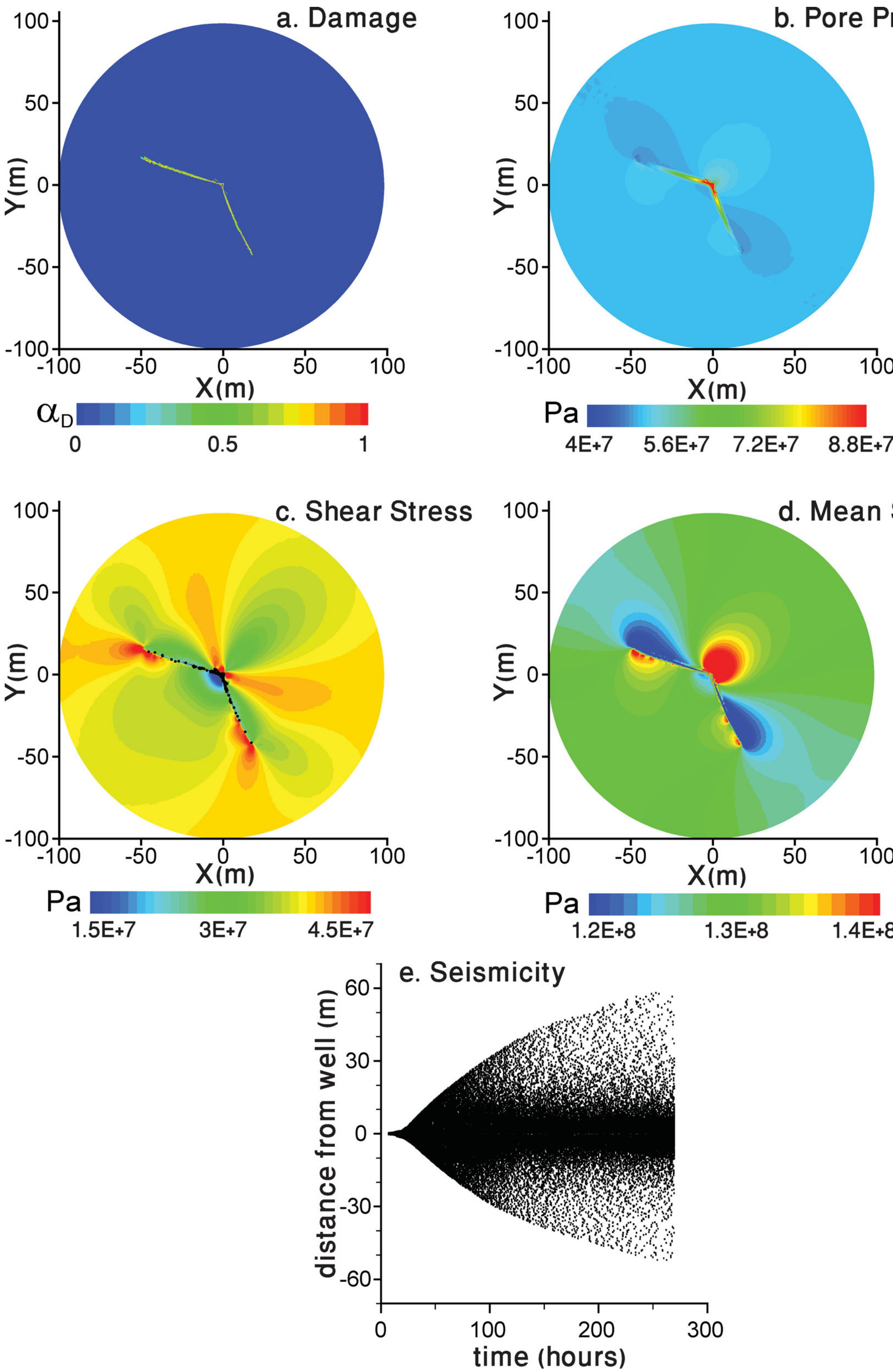

Figure 5. Results of the weak damage–permeability coupling scenario after 200 hr of injection. (a) Damage parameter (α_D), showing the formation of two damage zones. (b) Pore pressure within the damage zones increases due to fluid transport from the injection well and decreases closer to the tip of the damage zone because of dilatancy. Outside the damage zones, the pore pressure changes poro-elastically similar to the pattern of the mean stress. (c) Shear stress expressed as the second invariant of the stress tensor (J_2) and seismic events locations. (d) Mean stress. (e) r-t diagram of seismicity where the slope represent the velocity of damage propagation. Four stages are observed: (1) no seismicity, (2) damage acceleration, (3) constant velocity and (4) damage deceleration.

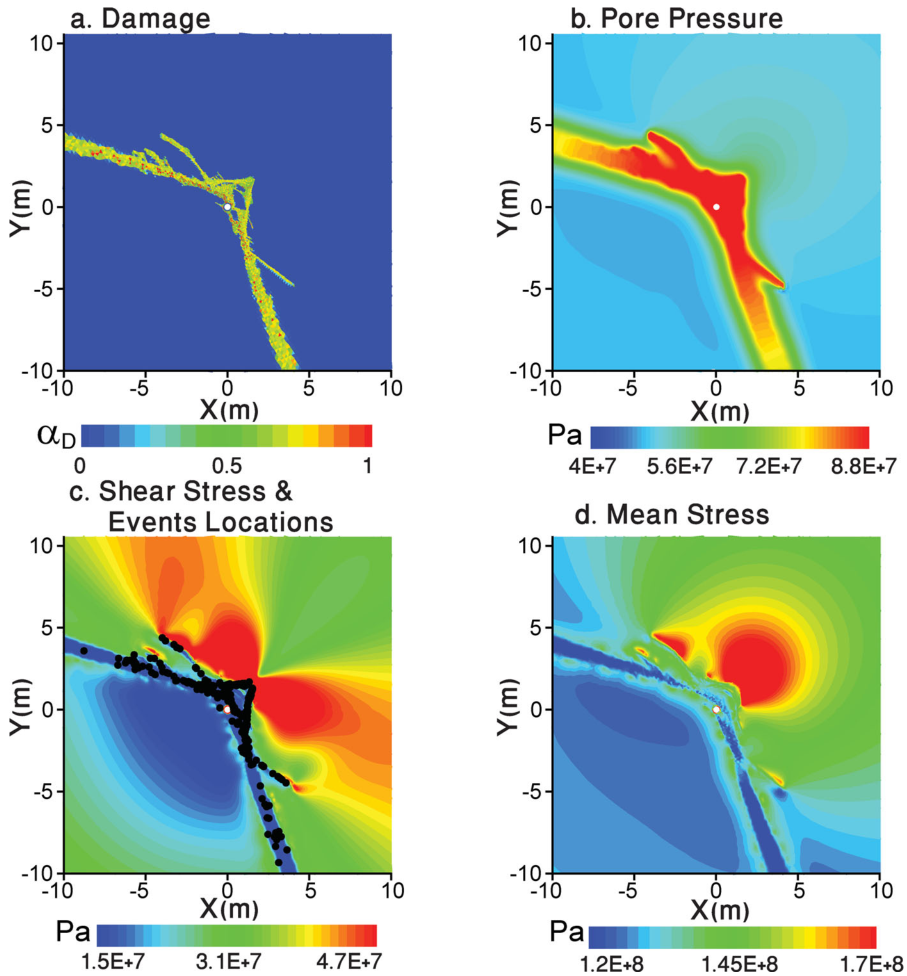

Figure 6. Results of the weak damage–permeability coupling scenario after 200 hr of injection close to the injection well. (a) Damage parameter (α_D), showing the formation of additional damage zones. (b) Pore pressure increases mainly within the damage zones by fluid transport from the injection well. (c) Shear stress within the damage zones is small because of softening of the damaged rocks. Seismic events occur only within the damage zones. (d) Mean stress within the damage zones is small because of softening of the damaged rocks.

are 10^{-19}m^2 and 10^{-14}m^2, respectively (five orders of magnitude), but only at high damage the permeability is high (Table 1). In this case, the two damage zones are the conjugate set with different orientations (Fig. 5). The choice of which conjugate system will progress and which will decay depends on random numerical noise. Seismicity starts about 7 hr after injection and damage acceleration stops after 30 hr. The different orientation of the two damage zones creates an angle at the injection well that concentrates stress. As a result, secondary damage zones develop at later stages around the well (Fig. 6). The mean and shear stresses within the damage zone is small because the damaged rock lost most of its stiffness and is too weak to hold large stress (Fig. 6). Outside the damage zone, the rock is undamaged and the stress reflects the elastic response to the deformation of the damage zone (Figs 6c and d). The pore pressure within the damage zone is high because their high permeability allows high pressure diffusion with the well. Outside the damage zone, the pore pressure changes only due to poro-elastic effects and has the same pattern as the mean stress. If, for the same conditions, the injection is shut down, the system re-stabilizes rapidly (Fig. 7). The seismicity rate decreases significantly, and damage progression decreases and finally stops after 170 hr (Fig. 7).

In the uncoupled scenario, permeability does not depend on damage and remains 10^{-14} m^2 (Fig. 8). Poro-elastic coupling (eqs 2

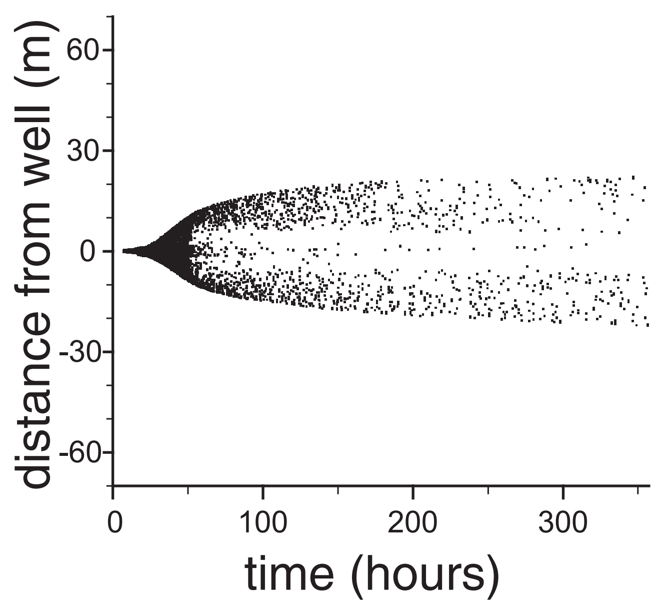

Figure 7. r-t diagram of seismicity of the weak damage–permeability coupling scenario when injection is stopped after 42 hr.

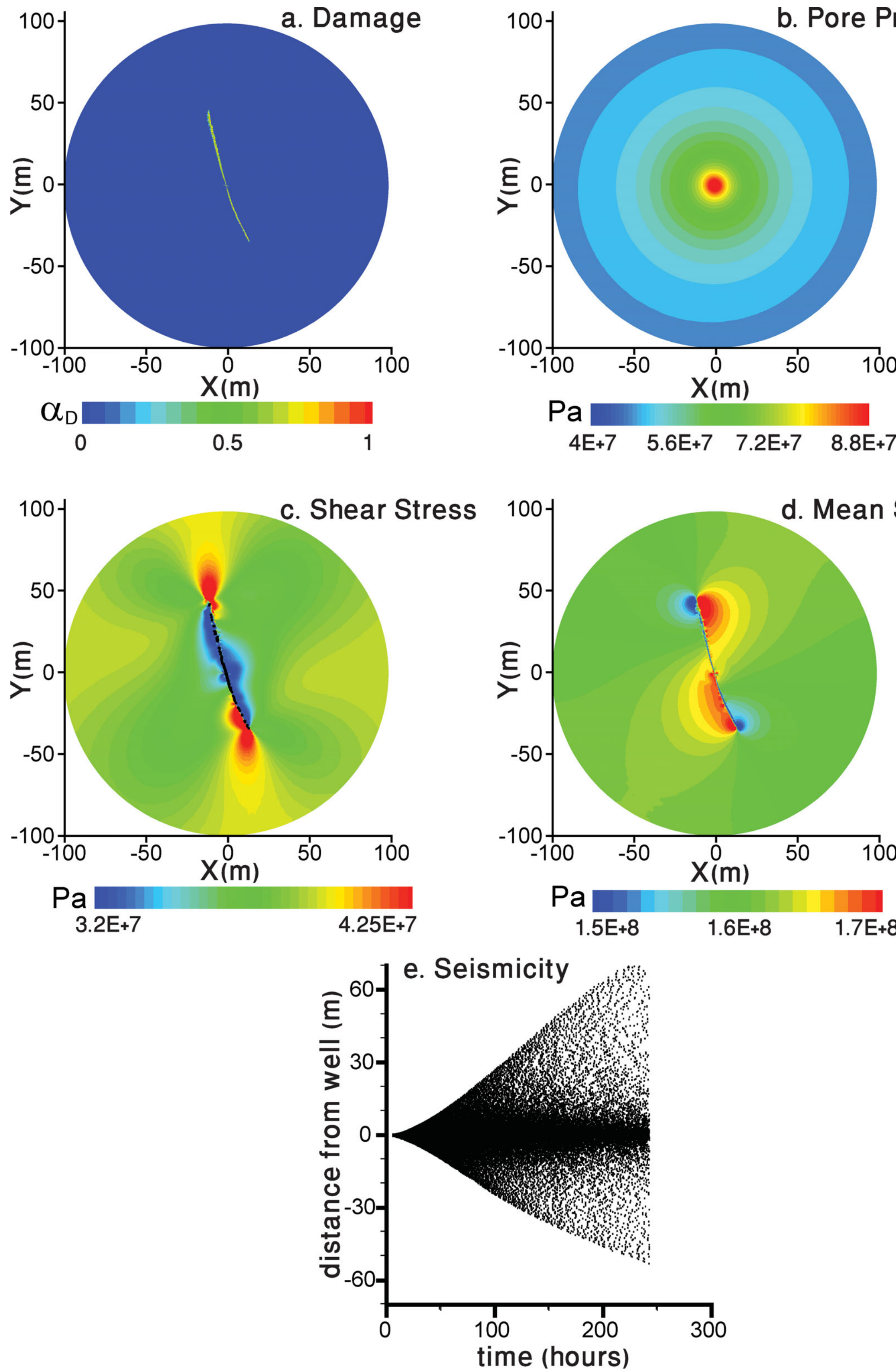

Figure 8. Results of the uncoupled damage/permeability scenario after 200 hr of injection. (a) Damage parameter (α_D), showing the formation of two damage zones. (b) Pore pressure increases radially. (c) Shear stress and seismic events locations. (d) Mean stress. (e) r-t diagram of seismicity. Four stages are observed: (1) no seismicity, (2) damage acceleration, (3) constant velocity and (4) damage deceleration.

and 5) during the injection creates damage that is coupled into the poro-elastic solution but without altering the permeability. Even this simplified scenario results in complicated damage propagation with acceleration until 100 hr of injection (Fig. 8e).

The evolution of the pore pressure within the damage zone depends on the permeability–damage relation (Fig. 9). In all cases dilatancy suction takes place as damage is advancing, but in most cases the enhanced permeability associated with the dilatancy

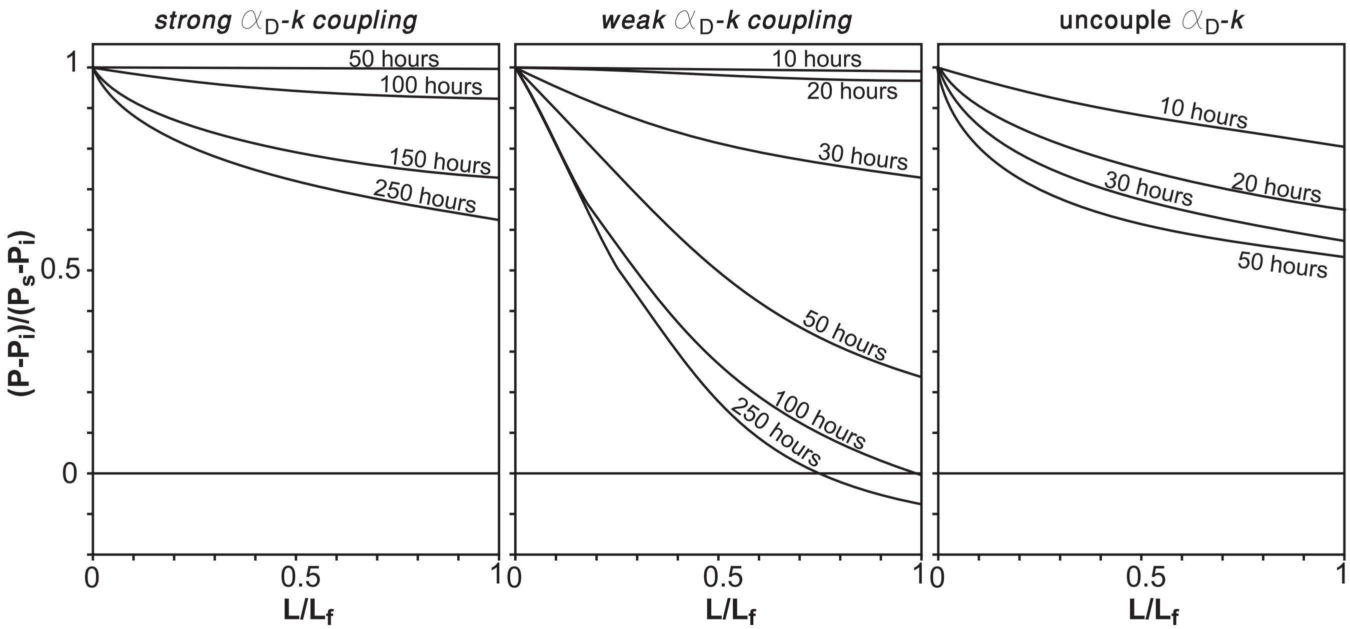

Figure 9. Normalized pore pressure along the damage zones, where P is the pore pressure, P_i is the initial pore pressure, P_s is the pore pressure at the injection well, L is the distance from the well within the damage zone, and L_f is the length of the damage zone (changes with time). In the strong damage–permeability coupling scenario pore pressure at the tip of the damage zone is 90 per cent of the source pressure after 100 hr. In the weak damage–permeability coupling scenario, pore pressure drops below the initial pore pressure after 250 hr because of dilatancy. In the uncoupled scenario, pore pressure within the damage zone drops rapidly to 80 per cent after 10 hr.

allows fast pressure diffusion from the injection well that increases the pore pressure. The weak damage–permeability coupling scenario is the only case where pore pressure diffusion could not compensate for the suction pressure reduction and after 250 hr the pore pressure at the tip of the damage zone is below the initial pore pressure (Fig. 9b). In the strong damage–permeability coupling scenario the pore pressure along the damage zone is never smaller than half of the injection pressure due to the high permeability maintained during injection (Fig. 9a).

High pore pressure preserved at the tip of the damage zone leads to an increase in the velocity of damage propagation proportional to the damage zone length (Fig. 10). Decrease of the pore pressure at the tip of the damage zone at the later stages leads to damage deceleration. Rapid drop of the pore pressure at the tip of the damage zone in the uncoupled scenario (Fig. 9c) leads to significantly slower acceleration of the propagating damage (Fig. 10). In the next section these results will be compared with predictions of the classical fracture mechanics models.

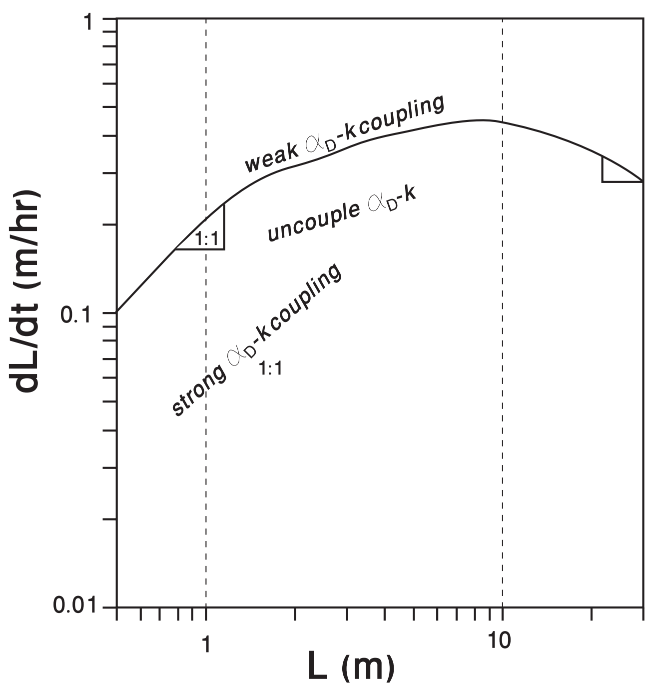

Figure 10. Log (velocity) versus the log (fracture's length) of the quasi-statically propagating damage.

4 DISCUSSION

Under constant remote loading, the stress intensity factor K_I increases proportionally to the square root of the fracture length, $\sqrt{L}$, leading to a power-law scaling relation between fracture velocity and its length, that is Charles (1958) or Paris & Erdogan (1963) law:

$$\frac{dL}{dt} = AL^{m/2}, \tag{7}$$

where A is a material parameter multiplied by the remote stress and the power-law index m is a material parameter. For $m = 2$, the growth law $d\ \ln(L) = Adt$ is completely scale-independent or 'complete similarity', is reached in the words of Barenblatt (1996). Experimental observations (e.g. Meredith & Atkinson 1985; Collins 1993) and microseismic data (Main *et al.* 1992, 1993) indicate that fracture propagation rate can be divided into three regimes. Propagation starts with $m = 2$–5 in the slow fracture corrosion regime I. In rocks, the exponent m decreases in regime II ($m < 2$), where fracture behavior is controlled by the rate of fluid transport to the fracture tip. The rupture in regime III is largely independent of environment and m increases steeply. Our numerical results fall into regimes I and II.

The duration of each regime depends on the ability of the damage zone to efficiently transport fluids to its tip. In the strong damage–permeability coupling scenario, damage accelerates for the first 110 hr and gets to a distance of 10 m from the well (Fig. 2e). This acceleration has a slope of 1 ($m = 2$) in log (velocity) over the log (length) plot of eq. 7 (Fig. 10). During this time the pressure at the tip of the damage zone is at least 90 per cent of the pressure at the injection well (Fig. 9a) and the propagation rate is damage-controlled (limited) according to predictions of fracture mechanics (eq. 7). After 110 hr, fluid transport is not efficient enough to preserve high pore pressure along the entire damage zone up to its tip in the long (>10 m) and narrow damage zone. Because the pore pressure at the tip of the damage zone is not high anymore, the propagation of damage decelerates. Power-law index m decreases and even becomes negative. During this stage the propagation rate is fluid transport controlled (limited).

In the weak damage–permeability coupling scenario the duration of regime I is shorter than in the strong damage–permeability coupling because the damage zone does not have the ability to efficiently transfer fluids from the injection well to the tip of the damage zone at relatively early stages. Damage accelerates for only the first 25 hr to a distance of 2.5 m from the well (Fig. 4e). Here also, the slope of the log (velocity) over the log (length) of the damage zone is one (Fig. 10). The pore pressure at the tip of the damage zone after 30 hr is less than 70 per cent of the pressure at the injection well (Fig. 9b). The damage zone propagation becomes fluid-limited at earlier stages compared to the strong damage–permeability coupling (Fig. 10). At later stages, that is after 250 hr, when the damage zones are longer than 30 m, the fluid transfer from the well to the tips of the damage zones could not keep up with dilation, and the pore pressure drops below the initial value (Fig. 9b). The slope of the log (velocity) over the log (length) becomes negative at this stage (Fig. 10).

With the lack of the damage–permeability coupling, the damage zone is propagating faster than the pore pressure. The pore pressure at the tip of the damage zone gradually decreases from the very initial stage (Fig. 9c). Therefore, the damage-controlled regime is so short that it cannot be recognized and the fluid transport is the major limiting factor controlling the growth rate; the power-law index is low; $m < 2$ (Fig. 10).

The value of the power-law index for the fluid-limited growth regime could be estimated using one-dimensional approximation for the fluid flow within the damage zone. Mass transport eq. (5) may be viewed as pressure-diffusion with diffusion coefficient $D = k/s_e$. The diffusion transport predicts that the distance that the pore pressure reaches during the time t is proportional to $L \sim \sqrt{Dt}$. Differentiation with respect to time gives the propagation velocity $dL/dt \sim 2\sqrt{D/t} \sim L^{-1}$. This estimation predicts that the power-law index in the complete fluid-limited regime should be $m = -1$ (Fig. 10). Such deceleration was observed during injection experiment in Soultz-sous-Forêts (Shapiro *et al.* 1999; their fig. 1) and in Fenton-hill (Langenbruch & Shapiro 2010; their fig. 9a).

5 CONCLUSIONS

All simulations show that the creation and propagation of damage zones could be divided into four stages. The duration of each stage depends on the hydrological and mechanical parameters.

(1) Fluid flow into the rock with no seismic events (5 to 20 hr). At this stage damage is initiated and two sets of conjugate damage zones are nucleated (four damage zones).

(2) Seismic events begin and accelerate for the next 20 to 70 hr. At the initial part of this stage, two of the damage zones create stress shadows on the other two damage zones that stop progressing. Pore pressure at the tip of the damage zone is >90 per cent of the pressure in the injection well. The velocity of the advancing damage is limited only by the rate of damage accumulation.

(3) Damage acceleration decreases. This stage lasts for the next 20 to 30 hr. Fluid transport becomes a limiting factor as the damage zones are too long to efficiently transfer the pressure from the well to their tip.

(4) Damage deceleration. In some cases the propagation stops. The propagation is controlled and limited by fluid transport from the injection well to the tip of the damage zone. Fluid transport does not keep up with the dilatancy of the damage zone.

The time and distance of propagation depend on the damage–permeability coupling (eq. 6) and the remote shear stress. Higher remote shear stresses cause shorter initial periods of no seismicity. Strong damage–permeability coupling causes longer acceleration stages. Some of this behavior was observed in Soultz-sous-Forêts and in Fenton Hill.

ACKNOWLEDGMENTS

We would like to thank the two anonymous reviewers, for the thorough evaluations of our manuscript. Gershon Kieval is thanked for kindly helping with editing the manuscript.

REFERENCES

Adachi, J., Siebrits, E., Peirce, A. & Desroches, J., 2007. Computer simulation of hydraulic fractures, *Int. J. Rock Mech. Min. Sci.,* **44,** 739–757.

Agnon, A. & Lyakhovsky, V., 1995. Damage distribution and localization during dyke intrusion, in *The Physics and Chemistry of Dykes,* pp. 65–78, eds Baer, G. & Heimann, A., Balkema, Rotterdam.

Allix, O. & Hild, F., 2002. *Continuum Damage Mechanics of Materials and Structures,* Elsevier, Amsterdam, p. 396.

Baisch, S., Vörös, R., Rothert, E., Stang, H., Jung, R. & Schellschmidt, R., 2010. A numerical model for fluid injection induced seismicity at Soultz-sous-Forêts, *Int. J. Rock. Mech. Min. Sci.,* **47,** 405–413.

Barenblatt, G.I., 1996. *Scaling, Self-Similarity and Intermediate Asymptotics,* Cambridge University Press, Cambridge.

Bercovici, D., Ricard, Y. & Schubert, G., 2001. A two-phase model for compaction and damage, Part 1: General theory, *J. Geophys. Res.,* **106,** 8887–8906.

Bercovici, D. & Ricard, Y., 2003. Energetics of a two phase model of lithospheric damage, shear localization and plate boundary formation, *Geophys. J. Int.,* **152,** 581–596.

Byerlee, J.D., 1978. Friction of rocks, *Pure Appl. Geophys.,* **116,** 615–626.

Charles, R.J., 1958. Static fatigue of glass, *J. Appl. Physics,* **29,** 1549–1560.

Collins, J.A., 1993. *Failure of Materials in Mechanical Design,* John Wiley, New York.

Cuenot, N., Dorbath, C. & Dorbath, L., 2008. Analysis of the microseismicity induced by fluid injections at the Hot Dry Rock site of Soultz-sous-Forets (Alsace, France): implications for the characterization of the geothermal reservoir properties, *Pure Appl. Geophys.,* **165,** 797–828.

Cundall, P.A., 1989. Numerical experiments on localization in frictional materials, *Ign. Arch.,* **59,** 148–159.

Dieterich, J.H. & Kilgore, B.D., 1996. Imaging surface contacts; power law contact distributions and contact stresses in quarts, calcite, glass, and acrylic plastic, *Tectonophysics,* **256,** 219–239.

Fischer, T., Hainzl, S., Eisner, L., Shapiro, S.A. & Le Calvez, J., 2008. Microseismic signatures of hydraulic fracture growth in sediment formations: Observations and modeling, *J. Geophys. Res.,* **113,** B02307.

Hamiel, Y., Lyakhovsky, V. & Agnon, A., 2004a. Coupled evolution of damage and porosity in poroelastic media: theory and applications to deformation of porous rocks, *Geophys. J. Int.,* **156,** 701–713.

Hamiel, Y., Liu, Y., Lyakhovsky, V., Ben-Zion, Y. & Lockner, D., 2004b. A visco-elastic damage model with applications to stable and unstable fracturing, *J. Geophys. Int.,* **159,** 1–11.

Hamiel, Y., Lyakhovsky, V., Stanchits, S., Dresen, G. & Ben-Zion, Y., 2009. Brittle deformation and damage-induced seismic wave anisotropy in rocks, *Geophys. J. Int.,* **178,** 901–909.

Hansen, N.R. & Schreyer, H.L., 1994. A thermodynamically consistent framework for theories of elasticity coupled with damage, *Int. J. Solids Struct.,* **31,** 359–389.

Häring, M.O., Schanz, U., Ladner, F. & Dyer, B., 2008. Characterization of the Basel 1 enhanced geothermal system, *Geothermics,* **37,** 469–495.

Hoff, N.J., 1953. The necking and rupture of rods subjected to constant tensile loads, *J. Appl. Mech.,* **20,** 105–108.

Hossain, M.M. & Rahman, M.K., 2008. Numerical simulation of complex fracture growth during tight reservoir stimulation by hydraulic fracturing, *J. Pet. Sci. Eng.,* **60,** 86–104.

Johnson, P.A. & Jia, X., 2005. Non-linear dynamics, granular media and dynamic earthquake triggering, *Nature,* **437,** 871–874.

Kachanov, L.M., 1958. On the time to rupture under creep conditions [in Rusian], *Izv. Akad. Nauk SSSR Otd. Tekh. Nauk,* **8,** 26–31.

Kachanov, L.M., 1986. *Introduction to Continuum Damage Mechanics,* Martinus Nijhoff, Dordrecht, Netherlands, p. 135.

Kachanov, M., 1994. On the concept of damage in creep and in the brittle-elastic range, *Int. J. Damage Mech.,* **3,** 329–337.

Kanamori, H. & Anderson, D.L., 1975. Theoretical basis of some empirical relations in seismology, *Bull. Seism. Soc. Am.,* **65,** 1073–1095.

Karrech, A., Regenauer-Lieb, K. & Poulet, T., 2011. Continuum damage mechanics for the lithosphere, *J. Geophys. Res.,* **116,** B04205.

King, G.C.P., Stein, R.S. & Lin, J., 1994. Static stress changes and the triggering of earthquakes, *Bull. Seism. Soc. Am.,* **84,** 935–953.

Kohl, T. & Megel, T., 2007. Predictive modeling of reservoir response to hydraulic stimulations at the European EGS site Soultz-sous-Fôrets, *Int. J. Rock. Mech. Min. Sci.,* **44,** 1118–1131.

Krajcinovic, D., 1996. *Damage Mechanics,* Elsevier, Amsterdam.

Langenbruch, C. & Shapiro, S.A., 2010. Decay rate of fluid-induced seismicity after termination of reservoir stimulations, *Geophysics,* **75,** MA53–MA62.

Lee, S.H. & Ghassemi, A., 2011. Three-dimensional thermo-poro-mechanical modeling of reservoir stimulation and induced microseismicity in geothermal reservoir, in *Thirty Sixth Workshop on Geothermal Reservoir Engineering,* Stanford University, Stanford, California, SGP-TR-191.

Lemaitre, J., 1996. *A Course on Damage Mechanics,* Springer, Berlin.

Lemaitre, J. & Desmorat, R., 2005. *Engineering Damage Mechanics: Ductile, Creep, Fatigue and Brittle Failures,* Springer, Berlin.

Lyakhovsky, V., Podladchikov, Y. & Poliakov, A., 1993. Rheological model of a fractured solid, *Tectonophysics,* **226,** 187–198.

Lyakhovsky, V., Ben-Zion, Y. & Agnon, A., 1997. Distributed damage, faulting, and friction, *J. Geophys. Res.,* **102,** 27 635–27 649.

Lyakhovsky, V., Ben-Zion, Y. & Agnon, A., 2005. A viscoelastic damage rheology and rate- and state-dependent friction, *Geophys. J. Int.,* **161,** 179–190.

Lyakhovsky, V. & Ben-Zion, Y., 2008. Scaling relations of earthquakes and aseismic deformation in a damage rheology model, *Geophys. J. Int.,* **172,** 651–662.

Main, I.G., Meredith, P.G. & Sammonds, P.R., 1992. Temporal variations in seismic event rate and b-values from stress corrosion constitutive laws, *Tectonophysics,* **211,** 233–246.

Main, I.G., Meredith, P.G. & Sammonds, P.R., 1993. Application of a modified Griffith criterion to the evolution of fractal damage during compressional rock failure, *Geophys. J. Int.,* **115,** 367–380.

Meredith, P.G. & Atkinson, B.K., 1985. Fracture toughness and subcritical crack growth during high-temperature tensile deformation of Westerly granite and Black gabbro, *Tectonophysics,* **39,** 33–51.

Newman, W.I. & Phoenix, S.L., 2001. Time-dependent fiber bundles with local load sharing, *Phys. Rev. E,* **63**(2), 021507.

Ortiz R., A.E., Renner, J. & Jung, R., 2011. Hydromechanical analyses of the hydraulic stimulation of borehole Basel 1, *Geophys. J. Int.,* **185,** 1266–1287.

Paris, P.C. & Erdogan, F., 1963. A critical analysis of crack propagation laws, *J. Basic Engineering, ASME Trans., Series D,* **85,** 528–534.

Pearson, C., 1981. The relationship between microseismicity and high pore pressures during hydraulic stimulation experiments in low permeability granitic rocks, *J. Geophys. Res.,* **86,** 7855–7864.

Picandet, V., Khelidj, A. & Bastian, G., 2001. Effect of axial compressive damage on gas permeability of ordinary and high performance concrete, *Cement. Concrete Res.,* **3,** 1525–1532.

Poliakov, A., Cundall, P., Podladchikov, Y. & Lyakhovsky, V., 1993. An explicit inertial method for the simulation of viscoelastic flow: an evaluation of elastic effects on diapiric flow in two- and three-layers model, in *Dynamic Modeling and Flow in the Earth and Planets,* Proceedings of the NATO Advanced Study Institute, pp. 175–195, eds Runcorn, K.E. & Stone, D., Kluwer, Dordrecht.

Rabotnov, Y.N., 1959. A mechanism of a long time failure, in *Creep Problems in Structural Members,* pp. 5–7, USSR Acad. of Sci. Publ., Moscow.

Rabotnov, Y.N., 1988. *Mechanics of Deformable Solids,* Nauka, Moscow, p. 712.

Ricard, Y. & Bercovici, D., 2003. Two-phase damage theory and crustal rock failure: the theoretical “void” limit, and the prediction of experimental data, *Geophys. J. Int.,* **155,** 1057–1064.

Robinson, E.L., 1952. Effect of temperature variation on the long-term rupture strength of steels, *Trans. Am. Soc. Mech. Eng.,* **174,** 777–781.

Scholz, C.H., 2002. *The Mechanics of Earthquakes and Faulting,* 2nd edn, p. 471, Cambridge Univ. Press, New York.

Shapiro, S.A., Audigane, P. & Royer, J.J., 1999. Large-scale in situ permeability tensor of rocks from induced microseismicity, *Geophys. J. Int.,* **137,** 207–213.

Shcherbakov, R. & Turcotte, D.L., 2003. Damage and self-similarity in fracture, *Theor. Appl. Fract. Mech.,* **39,** 245–258.

Šílený, J., Hill, D.P., Eisner, L. & Cornet, F.H., 2009. Non–double-couple mechanisms of microearthquakes induced by hydraulic fracturing, *J. Geophys. Res.,* **114,** B08307.

Tang, C.A., Tham, L.G., Lee, P.K.K., Yang, T.H. & Li, L.C., 2002. Coupled analysis of flow, stress and damage (FSD) in rock failure, *Int. J. Rock Mech. Min. Sci.,* **39,** 477–89.

Turcotte, D.L., Newman, W.I. & Shcherbakov, R., 2003. Micro and macroscopic models of rock fracture, *Geophys. J. Int.,* **152,** 718–728.

Wang, H.F., 2000. *Theory of Linear Poroelasticity with Applications to Geomechanics and Hydrogeology,* Princeton University Press, Princeton.

Wang, S.Y., Sun, L., Au, A.S.K., Yang, T.H. & Tang, C.A., 2009. 2D-numerical analysis of hydraulic fracturing in heterogeneous geo-materials, *Constr. Build Mater.,* **23,** 2196–2206.

Zhao, X. & Young, R.P., 2011. Numerical modeling of seismicity induced by fluid injection in naturally fractured reservoirs, *Geophysics,* **76,** WC167.

Zoback, M. & Harjes, H.-P., 1997. Injection-induced earthquakes and crustal stress at 9 km depth at the KTB deep drilling site, Germany, *J. Geophys. Res.,* **102,** 18 477–18 491.